PCCP

PAPER

View Article Online
View Journal | View Issue

Cite this: *Phys. Chem. Chem. Phys.*, 2019, **21**, 8559

Pathways of amyloid-beta absorption and aggregation in a membranous environment†

Abhilash Sahoo,[a] Hongcheng Xu[b] and Silvina Matysiak *[ab]

Received 3rd January 2019,
Accepted 27th March 2019

DOI: 10.1039/c9cp00040b

rsc.li/pccp

Aggregation of misfolded oligomeric amyloid-beta (Aβ) peptides on lipid membranes has been identified as a primary event in Alzheimer's pathogenesis. However, the structural and dynamical features of this membrane assisted Aβ aggregation have not been well characterized. The microscopic characterization of dynamic molecular-level interactions in peptide aggregation pathways has been challenging both computationally and experimentally. In this work, we explore differential patterns of membrane-induced Aβ 16–22 (K–L–V–F–F–A–E) aggregation from the microscopic perspective of molecular interactions. Physics-based coarse-grained molecular dynamics (CG-MD) simulations were employed to investigate the effect of lipid headgroup charge – zwitterionic (1-palmitoyl-2-oleoyl-*sn*-*glycero*-3-phosphocholine: POPC) and anionic (1-palmitoyl-2-oleoyl-*sn*-*glycero*-3-phospho-L-serine: POPS) – on Aβ 16–22 peptide aggregation. Our analyses present an extensive overview of multiple pathways for peptide absorption and biomechanical forces governing peptide folding and aggregation. In agreement with experimental observations, anionic POPS molecules promote extended configurations in Aβ peptides that contribute towards faster emergence of ordered β-sheet-rich peptide assemblies compared to POPC, suggesting faster fibrillation. In addition, lower cumulative rates of peptide aggregation in POPS due to higher peptide–lipid interactions and slower lipid diffusion result in multiple distinct ordered peptide aggregates that can serve as nucleation seeds for subsequent Aβ aggregation. This study provides an in-silico assessment of experimentally observed aggregation patterns, presents new morphological insights and highlights the importance of lipid headgroup chemistry in modulating the peptide absorption and aggregation process.

1 Introduction

Aberrant aggregation of peptides and proteins on cellular membranes has been associated with the pathogenesis of a number of neurodegenerative diseases such as Alzheimer's (AD), Parkinson's (PD) and Huntington's (HD) disease.[1–3] Alzheimer's disease, characterized by extra-cellular amyloid plaques[4–6] and intra-cellular neurofibrillary tangles,[7,8] is a significant social challenge which has affected 5.7 million people in the United States.[9] The amyloid cascade hypothesis for AD presents the aggregation of a 39–43 residue long intrinsically disordered peptide-amyloid beta (Aβ) as the trigger for a cascade of events culminating in neuronal deaths and dementia.[10,11] Multiple alloforms of Aβ peptides with an intrinsic tendency to form fibrillar aggregates are created by successive excisions of amyloid precursor proteins (APP) by beta secratase in the endosomal pathway and gamma secretase in the plasma membrane.[12–14] Recent evidence has implicated soluble, low molecular weight Aβ oligomers as the primary cytotoxic agents, correlating strongly with cognitive defects.[15–18] The structural diversity of polymorphic Aβ oligomers contributes towards multiple pathways for Aβ-induced neuronal toxicity.[19]

A broad range of proteins and peptides, regardless of large variations in the amino acid sequence, have been shown to form an amyloid fibril at high concentrations.[20–22] Experimental characterization of peptide aggregates by X-ray diffraction has revealed common structural features such as a cross beta sheet architecture.[23,24] Structural studies of Aβ peptides by solid state NMR,[25] hydrogen–deuterium exchange[26] and electron microscopy[27–29] have also shown the presence of similar cross beta sheet patterns. The central hydrophobic core (CHC), residues 17–21 (L–V–F–F–A) of the complete Aβ, is crucial for fibrillation.[30–34] In addition, solid state NMR studies have confirmed that Aβ 16–22 (K–L–V–F–F–A–E) is one of the the smallest peptide sequences capable of forming highly ordered, stable beta sheet rich fibrils at neutral pH.[35] Therefore studies

[a] *Biophysics Program, Institute of Physical Science and Technology, University of Maryland, College Park, MD, USA. E-mail: matysiak@umd.edu*
[b] *Fischell Department of Bioengineering, University of Maryland, College Park, MD, USA*

† Electronic supplementary information (ESI) available: Alterations to the coarse grained model and other supporting evidence. Movie presenting membrane assisted emergence of secondary structures on POPS. See DOI: 10.1039/c9cp00040b

of the structural and kinetic properties of a simpler tailorable model peptide, Aβ 16–22, can provide a better understanding of the molecular forces responsible for fibril formation/elongation.[36–38]

The production of Aβ peptides occurs in a membranous environment, exposing the peptides to a number of lipid–peptide interactions.[39] Also, the perturbation of cellular membranes, followed by ion-dysregulation due to oligomeric forms of Aβ peptides is hypothesized to be a central part of Aβ assisted AD pathology.[39–41] Therefore, a mechanistic understanding of bio-mechanical interactions of Aβ peptides with cellular membranes is necessary to gain insights into the Aβ cascade pathway. Aβ peptides have been shown to exhibit varying aggregation patterns on lipid bilayers depending on their structure and composition.[42–49] CD and Thioflavin T assay studies of unilamellar vesicles have revealed an accelerated aggregation of Aβ 16–28 peptides into ordered beta sheets on an anionic bilayer (DPPG) as compared to a zwitterionic bilayer (DPPC).[45] In addition, an AFM experiment using supported bilayers has shown that the disruption of zwitterionic membranes (DOPC) is higher than that of anionic membranes (DOPG) in presence of Aβ peptides.[43] Recent evidence from imaging studies using TEM, AFM and total internal reflection fluorescence microscopy has suggested that small unilamellar vesicles (SUVs) with a larger curvature promotes amyloid fibril formation when compared to large unilamellar vesicles.[50,51]

A morphological characterization of Aβ oligomers is difficult due to its transient and soluble nature.[52–54] On the other hand, computational studies, particularly molecular dynamics (MD) can be an ideal alternative to access this small time scale, transient behaviour.[55] Atomistic simulations often coupled with advanced sampling techniques have been extensively implemented to study small-scale peptide oligomerization in solution.[56–63] Some recent atomistic studies on peptide–lipid interactions have investigated pre-formed membrane-inserted oligomers and the very initial phases of oligomer–lipid interactions.[64–66] Due to high computational costs and sampling issues, atomistic simulations have not been used to study peptide aggregation on lipid bilayers starting from a solvated monomeric configuration. Coarse grained molecular dynamics (CG-MD), which provides a reduced resolution description of a system and significantly improved sampling of a protein conformational landscape is an effective tool to study complex systems with extended spatio-temporal scales,[67] specifically peptide aggregation starting from monomeric peptides. Many novel coarse grained force-fields (in-lattice and off-lattice) have successfully characterized the ordered amyloid aggregation.[68–73] PRIME 20, an intermediate resolution unbiased peptide coarse graining scheme has been implemented with discontinuous molecular dynamics (DMD) on many amyloidogenic sequences including Aβ peptides to study fibril formation in solution.[74] Zheng, *et al.* explored the aggregation free energy landscape of Aβ peptides using AWSEM-MD – a predictive coarse grained force-field.[75] A minimalistic, phenomenological model (Clafisch model) was implemented with a variable dihedral term to generate peptide aggregation on model vesicles.[69] Recently, another phenomenological coarse grained three bead-per-residue, amyloidogenic peptide model (Shea model) was employed with an implicit solvent to demonstrate spontaneous peptide aggregation into beta sheets on model lipid membranes.[70] These coarse graining techniques either have been designed only for peptides (PRIME20-Hall model) or do not provide peptide sequence/lipid type specificity (Clafisch and Shea models).

Here, we present a CG-MD study on partitioning, folding and aggregation dynamics of Aβ 16–22 peptides (K–L–V–F–F–A–E), in presence of model lipid bilayers composed with zwitterionic-POPC (1-palmitoyl-2-oleoyl-*sn-glycero*-3-phosphocholine) and anionic-POPS (1-palmitoyl-2-oleoyl-*sn-glycero*-3-phospho-L-serine) starting from their solvated monomeric state. We designed the peptide using a modified version of a prior-developed coarse grained model – Water-Explicit Polarizable PROtein Model (WEPPROM),[76,77] which generated secondary structures of small peptides from primary amino acid sequences without any built-in bias. Lipids were modeled by another slightly altered variant of a recently created Water-Explicit Polarizable MEMbrane (WEPMEM) model that could accurately reproduce dielectric properties in the lipid-headgroup (interface) region.[77,78] Physically, peptide aggregation involves an interplay between hydrophobic and hydrophilic effects, indicating the importance of precise modeling of electrostatic interactions.[79,80] The novelty of these models is the introduction of structural polarization at the peptide-backbone and lipid-headgroup which is necessary for studying peptide–lipid interactions and membrane induced peptide folding.[77] Both these models have been parameterized to use Yesylevskyy's polarizable water model.[81]

Outer neuronal cell membranes are extremely diverse with a wide variety of glycerophospholipids and ceramides.[82] Aβ peptides show an enhanced propensity to aggregate into ordered beta sheets on negatively charged membranes composed with anionic lipids.[45,79,83–86] Also, many experimental studies to understand the effect of lipid type on peptide aggregation have used POPS as one of the anionic components.[87–89] This prompts our choice of using POPS as the model anionic lipid to study the oligomerization of Aβ peptides in membraneous environments. In this paper we explore the differences in the morphology and kinetics of membrane-assisted beta sheet formation by Aβ 16–22 on model lipid membranes using coarse grained MD simulations. The paper also presents a mechanistic explanation for experimentally observed kinetic behaviour. To our knowledge, this is the first coarse grained simulation study that captures the complex process of peptide aggregation in a membraneous environment, from peptides solvated in their monomeric state to formation of ordered secondary structures, while maintaining a peptide sequence and lipid type specificity.

2 Methods

2.1 Peptide model

The Aβ peptide model is primarily derived from WEPPROM – which has been successfully applied to study interfacial folding and aggregation of small peptides without any externally added bias,[76,77] with certain modifications (Table S1, ESI†). In short,

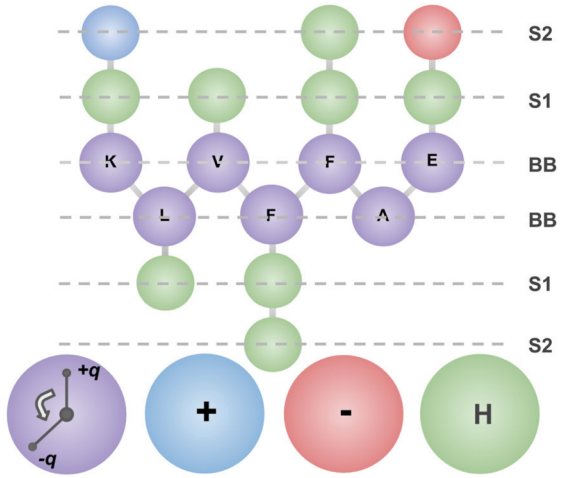

Fig. 1 A schematic description of the peptide coarse-grained model.

the CG peptide consists of three types of beads – charged (+/−), hydrophobic (H) and polar (P) mapped in an atomistic amino acid sequence (Fig. 1). Each amino acid's peptide backbone has been mapped into a single polarizable backbone bead (BB) with structural polarization added through dummy positive/negative charges (BBp/BBm). These dummy charges interact with the central backbone bead through a harmonic potential, with each other through a cosine squared angle potential and with their environment through electrostatic forces. This results in an induced-dipole effect, adding directionality to peptide backbone–backbone interactions, and generating secondary and super-secondary structures.[76] Charged residues (K and E) are represented as two side chain beads (S1/S2) – one hydrophobic and another charged. The side-chains in the CHC region (L–V–F–F) just have hydrophobic beads with the sidechains of leucine and valine represented as a single bead (S1) and phenylalanine as two beads (S1 and S2).

Further details about forcefield parameters, parametrization and model validation are provided by Ganesan *et al.*[76] and modifications are listed in the ESI† (Table S1).

The peptide model was validated using experimental and computational results of Aβ 16–22 aggregation into ordered cross beta structures in aqueous solution.[23,24,36,90] Simulations with 12 Aβ monomers solvated in water (0.14 M) aggregated into stable beta sheet rich oligomers (Fig. S1, ESI†).

2.2 Lipid model

Similar to the original MARTINI forcefield,[91] lipids – POPC and POPS in our lipid model – adapted from WEPMEM[77] are modelled by 13 CG beads each by a 4 : 1 mapping scheme. Some alterations made to the WEPMEM forcefield have been described in Table S2 (ESI†). At the lipid-headgroup, phosphate (PO4) and choline (NC3) are mapped to a charged coarse grained bead, whereas glycerol-esters (GL1 and GL2) and serine (CNO) are represented by polarizable beads with structural polarization generated through two dummy charges similar to the peptide model. Lipid oleoyl tails are designed with five hydrophobic beads, whereas the palmitoyl tails with four. Please refer to the study by Ganesan *et al.* for further description of the coarse grained model.[77] Both the lipid and peptide models are compatible with each other and use the polarizable MARTINI water model[81] for solvation.

2.3 Simulation protocol

The model POPC bilayer, composed with 240 lipids and POPS bilayer with 242 lipds were solvated with CG water (the water to lipid ratio fixed approximately to 20 : 1). The simulations were performed on GROMACS 4.5.4.[92] After the preliminary energy minimization, the bilayers and counter-ions (in the case of POPS bilayer) were equilibrated for 10 ns (time step, dt = 10 fs) using an *NPT* ensemble. Temperature was maintained at 300 K using a Noose–Hoover thermostat[93,94] with a time constant of 1 ps. Parinello–Rahman barostat[95] with a time constant of 1 ps and a compressibility of 3×10^{-5} bar^{-1} was used alongside with semi-isotropic pressure coupling to maintain a pressure of 1 bar. Particle mesh Ewald (PME)[96,97] with a relative dielectric constant of 2.5 and cutoff distance of 1.6 nm was used to compute long range electrostatics. The Lennard-Jones interactions were modified starting from 0.9 nm to 0 at 1.2 nm by the GROMACS shift scheme.

After creation of an equilibrated bilayer, 48 peptides (a peptide to lipid ratio of about 0.2) are randomly added into the solution. A peptide to lipid molar ratio of 1 : 5 has been previously investigated in small (Aβ 25–35) peptide-membrane experiments.[98] The composite system is then energy minimized and re-equilibrated for 50 ns with position restraints placed on 4th residue backbone (on F-19 BB in x, y an z directions) in peptides and phosphate (on PO4 in z direction) in lipids. The bilayers were simulated with a fixed surface tension (Berendsen barostat) to mimic an enhanced area per lipid due to the outer membrane curvature of SUVs. The area per lipid of both POPC and POPS bilayers was fixed at 95 Å^2 to simulate the outer membrane of a SUV with 13.4 nm diameter. These values were obtained from the WEPMEM simulation of a small unilamellar vesicle system composed of 877 lipids and 61113 CG-water molecules and also verified against other coarse grained molecular dynamics simulations with comparable vesicle sizes.[99,100] All other simulation parameters were kept similar to those of the first equillibration step. This second step allows us to equilibrate the monomeric peptides in the solution in presence of a lipid bilayer.

Finally, position restraints were removed and a production run of 1.5 μs was carried out using the remaining simulation parameters from the second equillibration step. To verify the statistics presented in this paper, we also simulated a replica of bilayer-peptide systems with different initial states.

2.4 Analysis

Built-in functions of GROMACS, analysis modules of Visual Molecular Dynamics[101] (VMD) and in-house developed scripts were used to analyze the molecular simulation trajectory.

2.4.1 Peptide absorption. The relative positions of two F-S2 beads on the lipid bilayer surface described by locally close (six nearest neighbors from the center of mass) phosphate (PO4) beads have been used as metrics to differentiate between

absorbed and unabsorbed peptides. To accommodate for the local curvature of lipid bilayers, the height of the bilayer surface (h) is determined by the average heights of six nearest PO4 beads to each individual peptide. The peptides are then categorized into three classes – completely absorbed (CA), partially absorbed (PA) and unabsorbed (UA) based on the positions of phenylalanine S2 (F-19/F-20 S2) on a single peptide chain. If the position of both F-S2 along bilayer normal (z) is less or equal to h, the peptide is classified as completely absorbed (CA) whereas if $z > h$, the peptides are considered unabsorbed (UA). Fig. S2 (ESI†) provides a schematic representation of this algorithm and the three classes of peptides differentiated on the basis of absorption on the bilayer surface.

2.4.2 Peptide-aggregate clusters. Peptide aggregation in the simulated systems was quantified by clustering the connected peptides. In this analysis, the peptides are described by main beads – BB, S1 and S2. This connectedness is established using distance cutoffs determined from the first peak of radial distribution functions ($g(r)$) between these beads (Fig. S3, ESI†). Two peptides are connected if they have at-least one pair of beads within their respective cutoff distance. These cutoffs are detailed in Table 1.

The number of peptide clusters, representing peptide aggregates at a particular time is computed by determining connected components. In addition, the peptide aggregates are also categorized into three groups based on absorption classes of component peptides – completely absorbed aggregates, partially absorbed aggregates and unabsorbed aggregates. A peptide-aggregate has been categorized as a completely absorbed aggregate, if all of its component peptides can be classified as either completely absorbed or partially absorbed. On the other hand, an aggregate is categorized as a partially absorbed aggregate, if at-least one of its component peptides can be classified as partially absorbed and at-least another one as unabsorbed. Finally, if all of the component peptides are marked as unabsorbed, then the peptide-aggregate is categorized as unabsorbed aggregate.

2.4.3 Beta sheet content. A backbone contact between two peptides is defined by an alignment of back-bond dipoles (BBm-BBp), characterized using a distance cut off of 2.5 nm between two oppositely charged BB-dummies. This distance was determined from the interaction peak of radial distribution function, $g(r)$, between opposite charged dummy particles. We considered two peptides as beta sheets, if they have at least five (71.5%) such backbone–backbone contacts and an end-to-end distance greater than 1.2 nm, similar to the beta sheet determination technique used by Lu *et al.*[90] The end-to-end length is the distance between the back-bone (BB) beads of flanking amino acids – K and E. The fraction of peptides in mutual beta sheets constitute the total beta sheet content.

Table 1 Distance cutoff between an interacting pair of beads for calculation of peptide-aggregate clusters

Interaction	Cutoff (nm)
BB–BB	0.45
BB–S1	0.40
BB–S2	0.61
S1–S1	0.65
S1–S2	0.42
S2–S2	0.70

3 Results and discussion

Fig. 2a shows the number of unabsorbed peptides over time whereas Fig. 2a-inset shows the variation in the number of partially absorbed aggregates with time. The peptides can partition into lipid membranes as individual monomers (Fig. 2b),

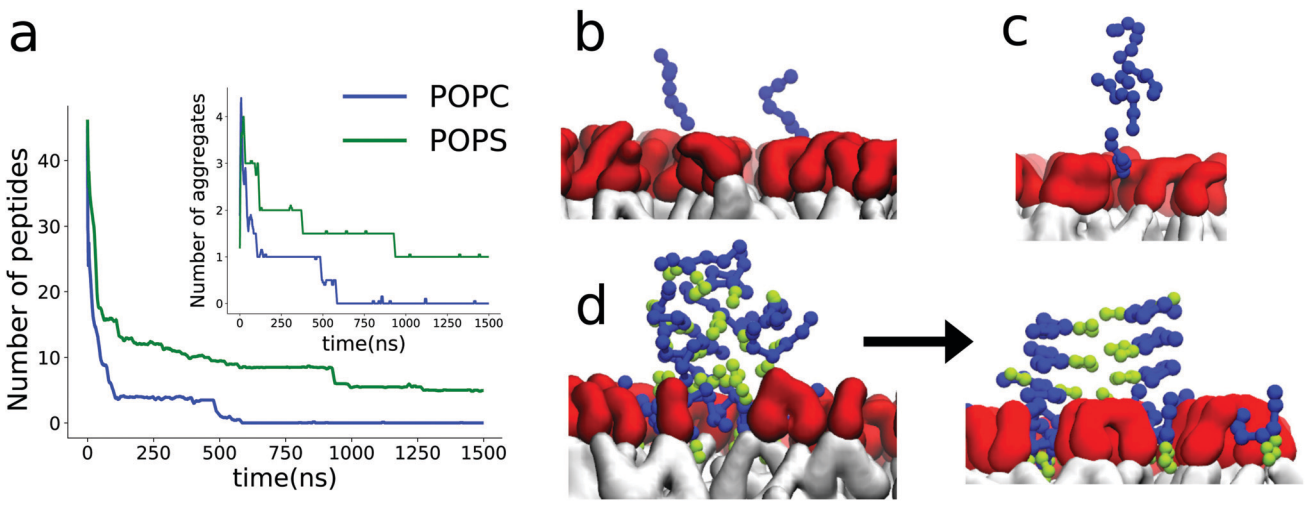

Fig. 2 (a) The variation in the number of "unabsorbed peptides" with time, averaged over two replica-simulations. The variation in the number of partially absorbed aggregates is shown as the inset. (b–d) Different pathways for peptide absorption into lipid bilayer. (b) Single (monomeric) peptide absorption. (c) Peptide absorption as oligomeric aggregates. (d) Peptide aggregation through dissociation and rearrangement of partially absorbed aggregates. Coloring scheme: light green beads – sidechains of phenylalanines (F); blue beads – peptide backbones; red region – the polar/charged lipid headgroup; white region – hydrophobic alkyl tails (lipids).

as small oligomeric aggregates (Fig. 2c) or by slow dissociation of larger peptide aggregations (Fig. 2d) bound to the lipid membrane. Previous AFM studies with full length Aβ peptides have also reported some of these pathways – absorption as monomers and oligomers into supported bilayers.[43] There was a sudden significant decrease in the number of unabsorbed peptides within about first 15 ns for both anionic-PS and zwitterionic-PC simulations (Fig. 2a). Following that, the absorption slowed down due to the formation of a number of partially absorbed aggregates. These aggregates arranged themselves to protect the hydrophobic cores of their component peptides (Fig. 2d), which afforded some stability and reduced absorption rates. Over time, these partially absorbed aggregates continued to slowly lose the peptides to the membrane and decrease in the total number and size. Particularly, in contrast to POPC where all the inter-facial aggregates were completely absorbed, one such aggregate on POPS rearranged and conformed into a stable layered beta sheet structure (Fig. 2d) attached to the membrane, similar to the structures observed in membrane-free systems (Fig. S1, ESI†).

The backbones of the absorbed peptides had variable residue-wise insertion into a lipid membrane modulated by their side chain hydrophobicity and relative positions along the peptide chain (Fig. S4, ESI†). Throughout the 1.5 μs simulation, the absorbed peptides remained close to the bilayer headgroup region (Fig. 2d and Fig. S6, ESI†). Once absorbed into the membrane, the peptides (monomers and aggregates) start diffusing laterally on the bilayer surface as shown in the supplementary movie (ESI†). In addition, as the peptides are pre-dominantly hydrophobic (71.43%), the aggregation on the membrane occurs primarily by pushing away the polar/charged lipid heads thereby exposing the hydrophobic tail region as is shown in Fig. 3a–d, where the peptides are pre-dominantly aggregated on top of the hydrophobic alkyl tails (white region).

3.1 Rate of peptide aggregation

The variation in the cumulative number of peptide clusters (ordered + disordered) over time is shown in Fig. 3e. Over time, due to the continued aggregation, the number of peptide

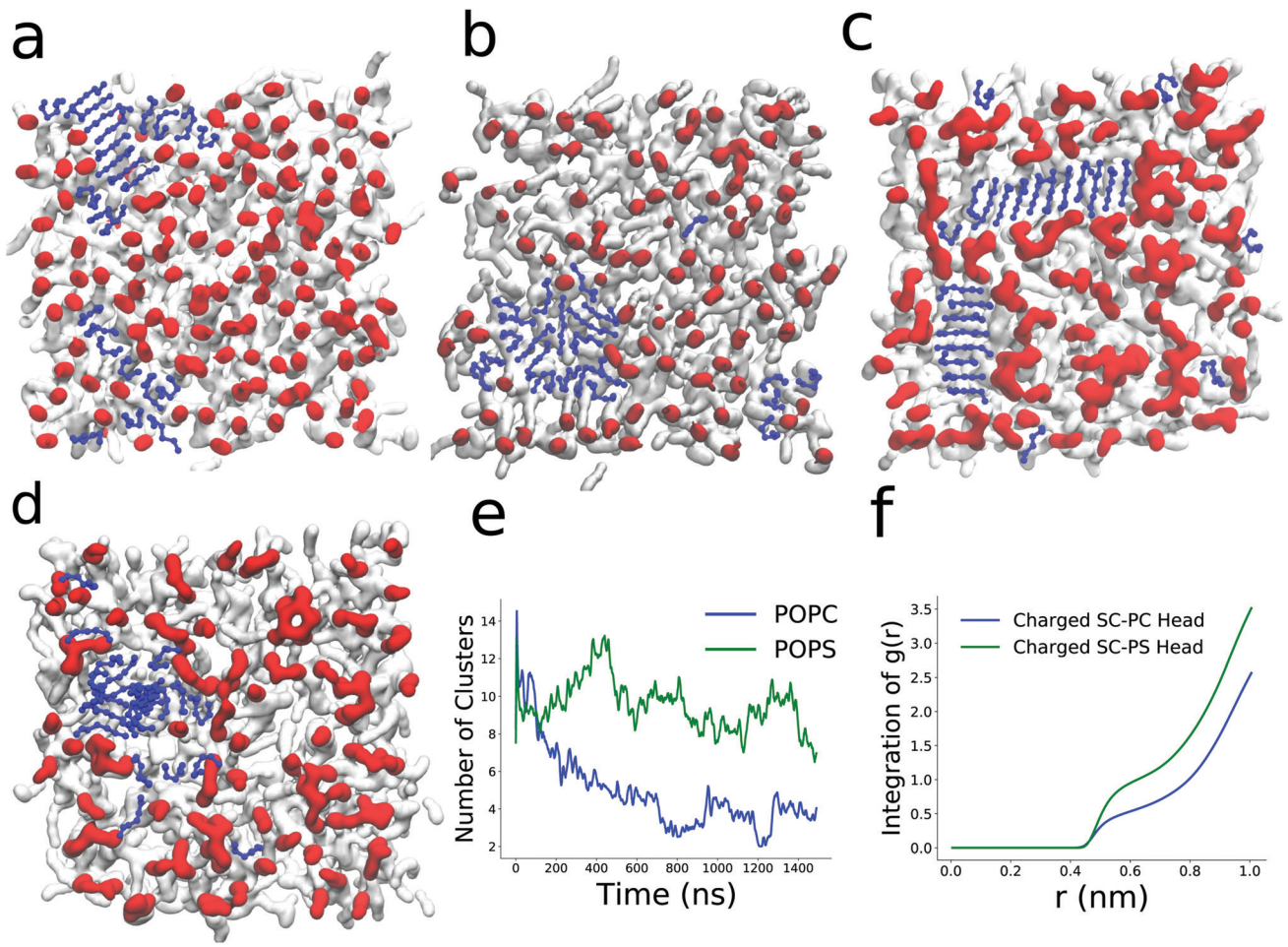

Fig. 3 (a and b) Last frame snapshot of peptide aggregates on two opposing leaflets of a POPC lipid membrane in simulation 1. (c and d) Last frame snapshot of peptide aggregates on two opposing leaflets of POPS lipid membrane in simulation 1. The red part in this representation corresponds to the polar headgroup and the white part corresponds to the hydrophobic tails. The blue connected beads represent the peptide backbone. (e) The variation in the number of Aβ 16–22 aggregates over time, averaged over both replica-simulations. Even monomers have been designated as individual peptide clusters. (f) Integration of radial distribution function between the charged peptide sidechains (E/K-S2) and lipid headgroup (POPC:NC3/PO4, POPS:CNO/PO4), averaged over both replica-simulations.

clusters on POPC steadily reduced in number (Fig. 3e) to about three clusters and increased in size – number of peptides (Fig. S5, ESI†). In contrast, on the POPS membrane, the number of peptide aggregates/clusters continued to be relatively high, featuring significant variations in aggregate sizes, pointing to a comparatively slower aggregation rate. This disparity in aggregation patterns can be explained through difference in the diffusion rates of PC and PS. Lateral diffusion of lipids is relatively slower in POPS with a lateral coarse grained diffusion constant of 0.0369×10^{-5} cm^2 s^{-1} as compared to 0.0899×10^{-5} cm^2 s^{-1} in POPC. While the coarse grained diffusion constant is not directly comparable to experimental and atomistic results, it can capture relative trends. A similar qualitative trend has also been observed in other reported values for lateral diffusion constants.[102] The rigid headgroup of POPS due to intra-molecular pseudo-hydrogen bonds captured by CNO dipole–dipole interactions in this coarse grained scheme prevents faster diffusion of lipids. This restricts the effective exclusion of lipid molecules,[77] preventing peptide aggregation. In addition, an increased interaction between the lipid head group (CNO/PO4) and peptides in POPS can further result in a better mixing of peptides and lipids, compared to that in POPC (Fig. 3f).

3.2 Beta sheet content

Over time, peptides rearranged into aggregates with a high beta sheet content on both bilayers. Fig. 4a shows time evolution of beta sheet content over time. Similar to reported CD and Thioflavin T assay studies[45] with Aβ 16–28, the beta sheet content in peptide aggregates was significantly larger (approximately double)

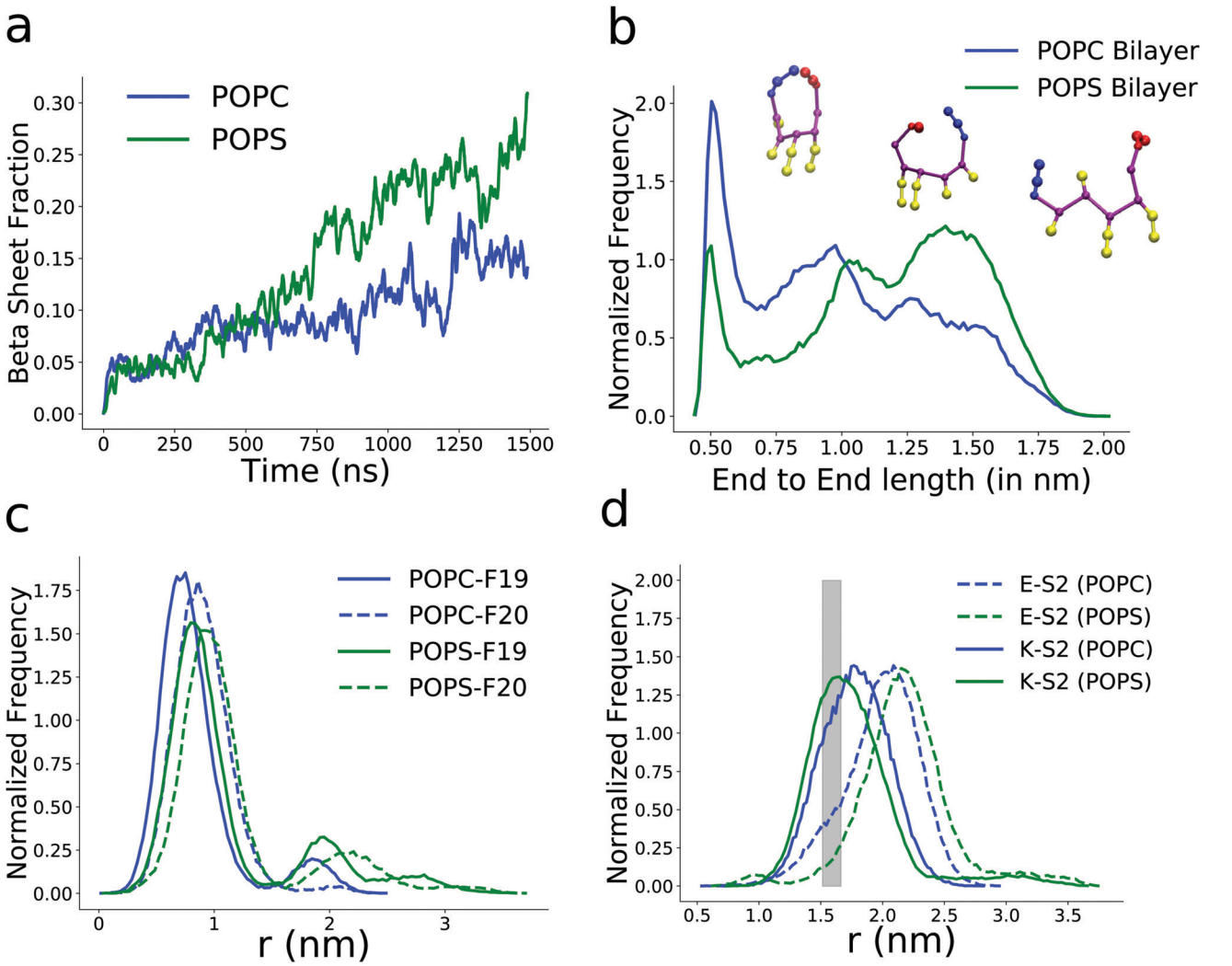

Fig. 4 (a) Time evolution of beta sheet fraction. (b) Distribution of end-to-end length of peptides over the last 200 ns. The gray line shows the end-to-end distance criteria used to determine beta sheets. (inset) Single peptide representative snapshots describing end-to-end lengths of peptides. Peptide backbone of Aβ 17-21 (LVFFA) is shown in magenta, whereas residues K and E are represented by blue and red respectively. The connected blue beads represent hydrophobic sidechains. (c) Density distribution of E-S2/K-S2 (POPC/POPS) along the bilayer normal from the bilayer center over the last 200 ns of simulation time. The gray region describes the average location of bilayer headgroup (PO4). (d) Density distribution of F19-S2/F20-S2 (POPC/POPS) beads along the bilayer normal from the bilayer center over last 200 ns of simulation time. All the results shown here have been averaged over all replica-simulations.

for POPS as compared to that for POPC. Even with larger sized aggregates, peptides on the PC bilayer were more unstructured. The higher beta sheet content on the PS bilayer can be explained by the distribution of the end-to-end distance of peptides. Peptides on PS are in general more elongated (Fig. 4b) which expose their backbone for more peptide backbone–backbone interactions, thereby increasing the overall beta sheet content. In agreement with our coarse grained simulations, atomistic molecular dynamics simulations of single peptide-membrane systems also reproduce a trend towards more elongated peptides in PS than in PC (Fig. S6, ESI†). This lower end-to-end distance of peptides in PC can be reasoned in terms of membrane compressibility and peptide–lipid insertion. The higher compressibility of POPC membranes as compared to that of POPS, that has been previously reported[103] and also captured by our CG model,[77] increases the relative penetration of peptides into POPC membranes. Fig. 4c shows the distribution of F-S2, the ''highest inserted'' side chain bead into the membrane. This increased insertion of F-S2 into POPC membranes, coupled with charged residues at the ends – K and E which prefer to stay close to the bilayer surface, distorts the shape of the peptide into a sharper ''U/O – like'' shape (Fig. 4b) thereby decreasing the average end-to-end distances and backbone-bone contacts. The higher membrane disruption of some zwitterionic lipids like DOPC compared to that of anionic DOPG has also been recorded in AFM experiments by Hane *et al.*[43] Moreover, similar to FTIR experiments on Aβ peptides in a membranous environment by Hu *et al.*,[104] a relatively higher insertion of F-19 as compared to that of F-20 is observed. In addition, as apparent from Fig. 4d the sidechain of Glutamate (E-S2) in POPS is positioned slightly away from the bilayer-headgroup as compared to that in POPC because of the interaction between positively charged choline (NC3) and negatively charged E-S2 which is absent in POPS. This further increases the possibility of intra-peptide K–E interactions which result in a less expanded peptide conformation.

In addition, due to the higher number of total inter-peptide interactions in large amorphous peptide aggregations on POPC, it is difficult for the peptides to effectively rearrange into ordered beta sheets necessary for efficient fibrillation. On the other hand, peptides on PS form numerous, slow diffusing smaller oligomeric aggregates which can reorganize comparatively easily into beta sheet rich structures before coalescing into larger aggregates.

Oligomeric deposits on membranes can act as nucleation-seeds for subsequent peptide aggregation in solution. To test this hypothesis, after the initial production run of 1.5 μs, we added 48 more peptides into both bilayer systems (with pre-existing peptide aggregates) and recorded their dynamics for 500 ns. Similar to previous experimental observations,[105] initial pre-existing oligomers acted as nucleating sites, recruiting either individual monomers or smaller oligomers to create large fibrillar aggregates (Fig. S7, ESI†). This opens a possibility of multiple ordered aggregates on POPS (larger than POPC) to act as nucleation sites that can progressively increase the subsequent aggregation rates. These fibrils are attached to the membranes primarily through inter-peptide interactions with embedded peptides and extend into solution. The aggregate sizes of fibrils in solution attached to the bilayers are on average larger than those of oligomers lying flat on membrane surfaces.

Studies on the central hydrophobic core (CHC) provide insights about how structures develop in peptide aggregates.[106–108] Faster development of ordered beta sheet rich structures in Aβ 16–22 can be corroborated with faster ordered fibrillation and the resulting toxicity of full length Aβ peptides in POPS. Similar to our observations, Lindberg *et al.*[109] also found about a twofold increase in the fibrillation of Aβ 1–42 in an anionic membrane (DOPS). This effect of lipid headgroup chemistry has also been validated in previous work with surface plasmon resonance and magnetic bead assay for Aβ 1–40.[110]

4 Conclusion

Our coarse grained molecular dynamics simulations reproduce and provide a mechanistic explanation for a broad spectrum of experimental results.[43,45,104,109,110] We characterized multiple pathways for peptide absorption into membranes composed of POPC and POPS. Both lipid molecules have distinct effects on aggregation patterns of absorbed peptides. While rapid cumulative aggregation (ordered + disordered) was observed in a zwitterionic PC bilayer, the emergence of ordered beta sheets and by extension, fibrillation was faster in presence of anionic POPS lipids. The results are in agreement with previous experimental studies[45,79,83–86,109,110] that had observed faster growth of amyloid fibrils in presence of anionic lipids. The discrepancy in the cumulative aggregation rates is a consequence of a faster lateral diffusion of POPC lipid molecules compared to that of POPS. On the other hand, increased beta sheet content in POPS membranes is due to the differences in membrane compressibility. A higher membrane compressibility of the POPC membrane compared to that of POPS, results in a relatively higher peptide insertion into the bilayer. This distorts the geometry of individual peptide molecules which hinders their participation in beta sheet formation. Some of the morphological aspects of membrane assisted Aβ aggregation reported in this study such as a relatively higher membrane insertion of F19 compared to that of F20, have been supported by previous experimental evidence.[104] We also revealed the propensity of initial oligomeric deposits to act as nucleation seeds to enhance further fibrillation. Considering the presence of multiple, ordered aggregates in POPS due to slow cumulative aggregation and peptide aggregates operating as nucleation seeds, POPS membranes can have increased progressive peptide aggregation rates. This work unravels how lipid headgroup driven biochemical interactions in homogeneous model membranes shape the peptide absorption and aggregation.

Conflicts of interest

There are no conflicts to declare.

Acknowledgements

This research was supported by the National Science Foundation under the Grant CHE-1454948 and through XSEDE

resources provided by the Texas Advanced Computing Center (TACC) under the grant number TG-MCB120045.

References

1 D. R. Howlett, K. H. Jennings, D. C. Lee, M. S. Clark, F. Brown, R. Wetzel, S. J. Wood, P. Camilleri and G. W. Roberts, *Neurodegeneration*, 1995, **4**, 23–32.
2 G. B. Irvine, O. M. El-Agnaf, G. M. Shankar and D. M. Walsh, *Mol. Med.*, 2008, **14**, 451–464.
3 M. Arrasate and S. Finkbeiner, *Exp. Neurol.*, 2012, **238**, 1–11.
4 G. G. Glenner and C. W. Wong, *Biochem. Biophys. Res. Commun.*, 1984, **122**, 1131–1135.
5 G. G. Glenner and C. W. Wong, *Biochem. Biophys. Res. Commun.*, 1984, **120**, 885–890.
6 C. L. Masters, G. Simms, N. A. Weinman, G. Multhaup, B. L. McDonald and K. Beyreuther, *Proc. Natl. Acad. Sci. U. S. A.*, 1985, **82**, 4245–4249.
7 C. Ballatore, V. M.-Y. Lee and J. Q. Trojanowski, *Nat. Rev. Neurosci.*, 2007, **8**, 663–672.
8 H. Braak and E. Braak, *Evolution of neuronal changes in the course of Alzheimer's disease*, Springer, Vienna, 1998, pp. 127–140.
9 Alzheimer's Association, *Alzheimers Dement*, 2018, **14**, 367–429.
10 B. Yankner, L. Dawes, S. Fisher, L. Villa-Komaroff, M. Oster-Granite and R. Neve, *Science*, 1989, **245**, 417–420.
11 D. J. Selkoe, *Neuron*, 1991, **6**, 487–498.
12 M. Goedert and M. G. Spillantini, *Science*, 2006, **314**, 777–781.
13 D. J. Selkoe, *Physiol. Rev.*, 2001, **81**, 741–766.
14 R. Tanzi, J. Gusella, P. Watkins, G. Bruns, P. St George-Hyslop, M. Van Keuren, D. Patterson, S. Pagan, D. Kurnit and R. Neve, *et al.*, *Science*, 1987, **235**, 880–884.
15 D. M. Walsh and D. J. Selkoe, *J. Neurochem.*, 2007, **101**, 1172–1184.
16 D. M. Walsh and D. J. Selkoe, *Neuron*, 2004, **44**, 181–193.
17 W. L. Klein, G. A. Krafft and C. E. Finch, *Trends Neurosci.*, 2001, **24**, 219–224.
18 C. C. Glabe, *Amyloid Accumulation and Pathogensis of Alzheimer's Disease: Significance of Monomeric, Oligomeric and Fibrillar Aβ*, Springer US, 2005, pp. 167–177.
19 J. Meinhardt, C. Sachse, P. Hortschansky, N. Grigorieff and M. Fändrich, *J. Mol. Biol.*, 2009, **386**, 869–877.
20 J. D. Gillmore, P. N. Hawkins and M. B. Pepys, *Br. J. Haematol.*, 1997, **99**, 245–256.
21 E. H. Koo, P. T. Lansbury and J. W. Kelly, *Proc. Natl. Acad. Sci. U. S. A.*, 1999, **96**, 9989–9990.
22 R. N. Rambaran and L. C. Serpell, *Prion*, 2008, **2**, 112–117.
23 K. L. Morris and L. C. Serpell, *Methods in Molecular Biology*, 2012, vol. 849, pp. 121–135.
24 M. Sunde, L. C. Serpell, M. Bartlam, P. E. Fraser, M. B. Pepys and C. C. Blake, *J. Mol. Biol.*, 1997, **273**, 729–739.
25 H. A. Scheidt, I. Morgado, S. Rothemund and D. Huster, *J. Biol. Chem.*, 2012, **287**, 2017–2021.
26 A. Olofsson, M. Lindhagen-Persson, M. Vestling, A. E. Sauer-Eriksson and A. Öhman, *FEBS J.*, 2009, **276**, 4051–4060.
27 V. L. Anderson and W. W. Webb, *BMC Biotechnol.*, 2011, **11**, 125.
28 C. Sachse, M. Fändrich and N. Grigorieff, *Proc. Natl. Acad. Sci. U. S. A.*, 2008, **105**, 7462–7466.
29 L. Gremer, D. Schölzel, C. Schenk, E. Reinartz, J. Labahn, R. B. G. Ravelli, M. Tusche, C. Lopez-Iglesias, W. Hoyer, H. Heise, D. Willbold and G. F. Schröder, *Science*, 2017, **358**, 116–119.
30 C. Hilbich, B. Kisters-Woike, J. Reed, C. L. Masters and K. Beyreuther, *J. Mol. Biol.*, 1992, **228**, 460–473.
31 H. Inouye, P. E. Fraser and D. A. Kirschner, *Biophys. J.*, 1993, **64**, 502–519.
32 D. A. Kirschner, H. Inouye, L. K. Duffy, A. Sinclair, M. Lind and D. J. Selkoe, *Proc. Natl. Acad. Sci. U. S. A.*, 1987, **84**, 6953–6957.
33 S. J. Wood, R. Wetzel, J. D. Martin and M. R. Hurle, *Biochemistry*, 1995, **34**, 724–730.
34 K. A. Ball, A. H. Phillips, P. S. Nerenberg, N. L. Fawzi, D. E. Wemmer and T. Head-Gordon, *Biochemistry*, 2011, **50**, 7612–7628.
35 J. J. Balbach, Y. Ishii, O. N. Antzutkin, R. D. Leapman, N. W. Rizzo, F. Dyda, J. Reed and R. Tycko, *Biochemistry*, 2000, **39**, 13748–13759.
36 A. K. Mehta, K. Lu, W. S. Childers, Y. Liang, S. N. Dublin, J. Dong, J. P. Snyder, S. V. Pingali, P. Thiyagarajan and D. G. Lynn, *J. Am. Chem. Soc.*, 2008, **130**, 9829–9835.
37 K. Lu, J. Jacob, P. Thiyagarajan, V. P. Conticello and D. G. Lynn, *J. Am. Chem. Soc.*, 2003, 6391–6393.
38 K. Tao, J. Wang, P. Zhou, C. Wang, H. Xu, X. Zhao and J. R. Lu, *Langmuir*, 2011, **27**, 2723–2730.
39 M. P. Murphy and H. I. LeVine, *J. Alzheimer's Dis.*, 2010, **19**, 311–323.
40 A. Itkin, V. Dupres, Y. F. Dufrêne, B. Bechinger, J.-M. Ruysschaert and V. Raussens, *PLoS One*, 2011, **6**, e18250.
41 A. Demuro, I. Parker and G. E. Stutzmann, *J. Biol. Chem.*, 2010, **285**, 12463–12468.
42 E. Drolle, A. Negoda, K. Hammond, E. Pavlov and Z. Leonenko, *PLoS One*, 2017, **12**, e0182194.
43 F. Hane, E. Drolle, R. Gaikwad, E. Faught and Z. Leonenko, *J. Alzheimer's Dis.*, 2011, **26**, 485–494.
44 M. Vestergaard, T. Hamada and M. Takagi, *Biotechnol. Bioeng.*, 2008, **99**, 753–763.
45 N. Sureshbabu, R. Kirubagaran, H. Thangarajah, E. J. P. Malar and R. Jayakumar, *J. Mol. Neurosci.*, 2010, **41**, 368–382.
46 J. A. Lemkul and D. R. Bevan, *Protein Sci.*, 2011, **20**, 1530–1545.
47 I. Morgado and M. Garvey, *Lipids in Amyloid-β processing aggregation and toxicity*, Springer, Cham, 2015, pp. 67–94.
48 L. Dominguez, L. Foster, J. E. Straub and D. Thirumalai, *Proc. Natl. Acad. Sci. U. S. A.*, 2016, **113**, E5281–E5287.
49 K. Matsuzaki, *Biochim. Biophys. Acta, Biomembr.*, 2007, **1768**, 1935–1942.

50 M. S. Terakawa, Y. Lin, M. Kinoshita, S. Kanemura, D. Itoh, T. Sugiki, M. Okumura and Y.-H. Lee, *Biochim. Biophys. Acta, Biomembr.*, 2018, **1860**, 1741–1764.
51 Y. Sugiura, K. Ikeda and M. Nakano, *Langmuir*, 2015, **31**, 11549–11557.
52 W. Yu, K. Zou, J. S. Gong, M. Ko, K. Yanagisawa and M. Michikawa, *J. Neurosci. Res.*, 2005, **80**, 114–119.
53 D. M. Walsh, A. Lomakin, G. B. Benedek, M. M. Condron and D. B. Teplow, *J. Biol. Chem.*, 1997, **272**, 22364–22372.
54 R. Kayed, E. Head, J. L. Thompson, T. M. McIntire, S. C. Milton, C. W. Cotman and C. G. Glabel, *Science*, 2003, **300**, 486–489.
55 P. Das, S. Matysiak and J. Mittal, *ACS Cent. Sci.*, 2018, **4**, 534–542.
56 R. Wu, J. Liu, X. Qiu and M. Deng, *Mol. Simul.*, 2017, **43**, 1227–1239.
57 B. Urbanc, L. Cruz, F. Ding, D. Sammond, S. Khare, S. Buldyrev, H. Stanley and N. Dokholyan, *Biophys. J.*, 2004, **87**, 2310–2321.
58 M. Biancalana and S. Koide, *Biochim. Biophys. Acta, Proteins Proteomics*, 2010, **1804**, 1405–1412.
59 N. G. Sgourakis, M. Merced-Serrano, C. Boutsidis, P. Drineas, Z. Du, C. Wang and A. E. Garcia, *J. Mol. Biol.*, 2011, **405**, 570–583.
60 N. G. Sgourakis, Y. Yan, S. A. McCallum, C. Wang and A. E. Garcia, *J. Mol. Biol.*, 2007, **368**, 1448–1457.
61 N. Nishikawa, P. H. Nguyen, P. Derreumaux and Y. Okamoto, *Mol. Simul.*, 2015, **41**, 1041–1044.
62 D. K. Klimov and D. Thirumalai, *Structure*, 2003, **11**, 295–307.
63 S. Santini, N. Mousseau and P. Derreumaux, *J. Am. Chem. Soc.*, 2004, **126**, 11509–11516.
64 C. H. Davis and M. L. Berkowitz, *Biophys. J.*, 2009, **96**, 785–797.
65 L. N. Zhao, S.-W. Chiu, J. Benoit, L. Y. Chew and Y. Mu, *J. Phys. Chem. B*, 2011, **115**, 12247–12256.
66 A. Brown and D. Bevan, *Biophys. J.*, 2016, **111**, 937–949.
67 S. Kmiecik, D. Gront, M. Kolinski, L. Wieteska, A. E. Dawid and A. Kolinski, *Chem. Rev.*, 2016, **116**, 7898–7936.
68 S. Abeln, M. Vendruscolo, C. M. Dobson and D. Frenkel, *PLoS One*, 2014, **9**, e85185.
69 R. Friedman, R. Pellarin and A. Caflisch, *J. Mol. Biol.*, 2009, **387**, 407–415.
70 A. Morriss-Andrews, F. L. H. Brown and J.-E. Shea, *J. Phys. Chem. B*, 2014, **118**, 8420–8432.
71 M. Chiricotto, T. T. Tran, P. H. Nguyen, S. Melchionna, F. Sterpone and P. Derreumaux, *Isr. J. Chem.*, 2017, **57**, 564–573.
72 Y. Chebaro, S. Pasquali and P. Derreumaux, *J. Phys. Chem. B*, 2012, **116**, 8741–8752.
73 M. Cheon, I. Chang and C. K. Hall, *Proteins*, 2010, **78**, 2950–2960.
74 M. Cheon, M. Kang and I. Chang, *Sci. Rep.*, 2016, **6**, 38196.
75 W. Zheng, M.-Y. Tsai, M. Chen and P. G. Wolynes, *Proc. Natl. Acad. Sci. U. S. A.*, 2016, **113**, 11835–11840.
76 S. J. Ganesan and S. Matysiak, *J. Chem. Theory Comput.*, 2014, **10**, 2569–2576.
77 S. J. Ganesan, H. Xu and S. Matysiak, *Phys. Chem. Chem. Phys.*, 2016, **18**, 17836–17850.
78 S. J. Ganesan, H. Xu and S. Matysiak, *J. Phys. Chem. B*, 2017, **121**, 787–799.
79 C. Ege, J. Majewski, G. Wu, K. Kjaer and K. Y. C. Lee, *ChemPhysChem*, 2005, **6**, 226–229.
80 S. J. Ganesan and S. Matysiak, *Phys. Chem. Chem. Phys.*, 2016, **18**, 2449–2458.
81 S. O. Yesylevskyy, L. V. Schäfer, D. Sengupta and S. J. Marrink, *PLoS Comput. Biol.*, 2010, **6**, e1000810.
82 R. O. Calderon, B. Attema and G. H. DeVries, *J. Neurochem.*, 2002, **64**, 424–429.
83 X. Yu, Q. Wang, Q. Pan, F. Zhou and J. Zheng, *Phys. Chem. Chem. Phys.*, 2013, **15**, 8878.
84 J. McLaurin and A. Chakrabartty, *Eur. J. Biochem.*, 1997, **245**, 355–363.
85 E. Terzi, G. Hoelzemann and J. Seelig, *Biochemistry*, 1994, **33**, 7434–7441.
86 E. Terzi, G. Hölzemann and J. Seelig, *Biochemistry*, 1997, 14845–14852.
87 C. Canale, S. Seghezza, S. Vilasi, R. Carrotta, D. Bulone, A. Diaspro, P. L. San Biagio and S. Dante, *Biophys. Chem.*, 2013, **182**, 23–29.
88 M.-A. Sani, J. D. Gehman and F. Separovic, *FEBS Lett.*, 2011, **585**, 749–754.
89 T.-L. Lau, J. D. Gehman, J. D. Wade, K. Perez, C. L. Masters, K. J. Barnham and F. Separovic, *Biochim. Biophys. Acta, Biomembr.*, 2007, **1768**, 2400–2408.
90 Y. Lu, P. Derreumaux, Z. Guo, N. Mousseau and G. Wei, *Proteins*, 2009, **75**, 954–963.
91 S. J. Marrink, H. J. Risselada, S. Yefimov, D. P. Tieleman and A. H. de Vries, *J. Phys. Chem. B*, 2007, 7812–7824.
92 S. Pronk, S. Páll, R. Schulz, P. Larsson, P. Bjelkmar, R. Apostolov, M. R. Shirts, J. C. Smith, P. M. Kasson, D. van der Spoel, B. Hess and E. Lindahl, *Bioinformatics*, 2013, 845–854.
93 S. Nosé, *Mol. Phys.*, 1984, **52**, 255–268.
94 W. G. Hoover, *Phys. Rev. A: At., Mol., Opt. Phys.*, 1985, **31**, 1695–1697.
95 M. Parrinello and A. Rahman, *J. Appl. Phys.*, 1981, **52**, 7182–7190.
96 T. Darden, D. York and L. Pedersen, *J. Chem. Phys.*, 1993, **98**, 10089–10092.
97 U. Essmann, L. Perera, M. L. Berkowitz, T. Darden, H. Lee and L. G. Pedersen, *J. Chem. Phys.*, 1995, **103**, 8577–8593.
98 N. Kandel, T. Zheng, Q. Huo and S. A. Tatulian, *J. Phys. Chem. B*, 2017, **121**, 10293–10305.
99 S. J. Marrink and A. E. Mark, *J. Chem. Phys.*, 2003, 15233–15242.
100 C.-M. Lin, C.-S. Li, Y.-J. Sheng, D. T. Wu and H.-K. Tsao, *Langmuir*, 2012, **28**, 689–700.
101 W. Humphrey, A. Dalke and K. Schulten, *J. Mol. Graphics*, 1996, **14**, 33–38.
102 F. E. Herrera and S. Pantano, *J. Chem. Phys.*, 2012, **136**, 015103.
103 J. Pan, X. Cheng, L. Monticelli, F. A. Heberle, N. Kučerka, D. P. Tieleman and J. Katsaras, *Soft Matter*, 2014, **10**, 3716.

104 Y. Hu, P. Kienlen-Campard, T.-C. Tang, F. Perrin, R. Opsomer, M. Decock, X. Pan, J.-N. Octave, S. N. Constantinescu and S. O. Smith, *Sci. Rep.*, 2017, **7**, 17159.
105 N. R. Anthony, A. K. Mehta, D. G. Lynn and K. M. Berland, *Soft Matter*, 2014, **10**, 4162–4172.
106 S. Chimon, M. A. Shaibat, C. R. Jones, D. C. Calero, B. Aizezi and Y. Ishii, *Nat. Struct. Mol. Biol.*, 2007, **14**, 1157–1164.
107 N.-V. Buchete and G. Hummer, *Biophys. J.*, 2007, **92**, 3032–3039.
108 J. Li, R. Liu, K. S. Lam, L.-W. Jin and Y. Duan, *Biophys. J.*, 2011, **100**, 1076–1082.
109 D. J. Lindberg, E. Wesén, J. Björkeroth, S. Rocha and E. K. Esbjörner, *Biochim. Biophys. Acta, Biomembr.*, 2017, **1859**, 1921–1929.
110 J. J. Kremer and R. M. Murphy, *J. Biochem. Biophys. Methods*, 2003, **57**, 159–169.

